ELSEVIER

Radiotherapy and Oncology 48 (1998) 293–305

RADIOTHERAPY & ONCOLOGY
JOURNAL OF THE EUROPEAN SOCIETY FOR THERAPEUTIC RADIOLOGY AND ONCOLOGY

Secondary neutron and photon dose in proton therapy

Stefano Agosteo[a,b,*], Claudio Birattari[b,c], Marcello Caravaggio[c], Marco Silari[d], Giampiero Tosi[e]

[a]*Dipartimento di Ingegneria Nucleare, Politecnico di Milano, via Ponzio 34/3, 20133 Milano, Italy*
[b]*Istituto Nazionale di Fisica Nucleare, Sezione di Milano, via Celoria 16, 20133 Milano, Italy*
[c]*Università degli Studi di Milano, Dipartimento di Fisica, via Celoria 16, 20133 Milano, Italy*
[d]*CERN, 1211 Geneve 23, Switzerland*
[e]*Istituto Europeo di Oncologia, via Ripamonti 435, 20141 Milano, Italy*

Received 14 August 1997; revised version received 15 April 1998; accepted 30 April 1998

Abstract

Background and purpose: The dose due to secondary neutrons and photons in proton therapy was estimated with Monte Carlo simulations. Three existing facilities treating eye and deep-seated tumours were taken into account. The results of the calculations related to eye proton therapy were verified with measurements.

Materials and methods: The simulations were performed with the FLUKA code. Neutron fluence was measured inside an Alderson phantom (type ART) with activation techniques.

Results: The maximum dose due to secondaries produced in a passive beam delivery system was estimated to be of the order of 10^{-4} and 10^{-2} Gy per therapy Gy for eye and deep tumour treatments, respectively. In the case of irradiations of deep-seated tumours carried out with an active system, the dose was of the order of 10^{-3} Gy per therapy Gy.

Conclusions: The dose due to secondaries depends on the geometry of the beam delivery system and on the energy of the primary beam and is lower in the healthy tissues distant from the target volume. © 1998 Elsevier Science Ireland Ltd. All rights reserved

Keywords: Proton therapy; Secondary neutron production; Monte Carlo simulations

1. Introduction

The estimate of the secondary neutron and photon dose absorbed by a patient irradiated with protons was required in the course of the design study, which was recently completed, of the Centro Nazionale di Adroterapia Oncologica (CNAO, National Centre of Oncological Hadrontherapy), a hospital-based proton and light-ion therapy facility in Italy [4–6,9]. It should be mentioned that the recent Italian regulation of radiation protection requires a personal archive of the global dose absorbed by patients during medical applications. The unwanted dose delivered to healthy tissues by secondaries produced both in the structural components of the accelerator and in the patient himself should be taken into account in the computation of the effective dose equivalent. This estimate could provide guidelines for the design of the beam transport system.

The literature dealing with the photoneutron dose in conventional X-ray radiation therapy is very exhaustive. The ambient dose equivalent was estimated to be in the range of 0.1–5 mSv per prescribed Gy at 1 m from the isocentre [2,18,25–28,33,36–38], depending on the considered accelerator and on the irradiation field. Moreover, the dose due to photoneutrons produced in a soft tissue phantom irradiated by 25 MV X-rays was estimated to be lower than 40 μGy per therapy Gy [1,19]. On the other hand, literature referring to secondaries produced in proton therapy is scarce. Secondary dose measurements were performed at the National Accelerator Centre (Faure, South Africa) [7], giving values of the order of 10^{-2} Gy per therapy Gy.

The production of secondaries strongly depends on the geometry and on the materials of the proton beam delivery system and it is almost impossible to refer to a standard configuration. In the present work, three different existing

* Corresponding author. Dipartimento di Ingegneria Nucleare, Politecnico di Milano, via Ponzio 34/3, 20133 Milano, Italy.

0167-8140/98/$19.00 © 1998 Elsevier Science Ireland Ltd. All rights reserved
PII S0167-8140(98)00049-8

configurations were considered, namely those in use at the proton therapy facilities of the National Accelerator Centre (Faure, South Africa) and of the Paul Scherrer Institute (PSI, Villigen, Switzerland) and the eye irradiation system installed at the Centre Antoine-Lacassagne (CAL, Nice, France). The secondary neutron and photon dose was estimated with Monte Carlo simulations using the FLUKA code [11–16]. This code transports hadrons and leptons from thermal energies up to several TeV and treats both hadronic and electromagnetic showers. Below 5 GeV, secondary hadron production is performed with the intranuclear cascade model, followed by pre-equilibrium emission, nuclear evaporation/fragmentation and residual nucleus deexcitation with photon emission.

A detailed computational phantom was used in the calculations related to eye irradiation while simpler models were adopted in the simulations of deep tumour treatment. Measurements of neutron fluence rates inside an Alderson phantom were performed at the CAL to verify the simulation results related to the eye irradiation.

2. Simulation features

The main characteristics of the simulation geometry are briefly described in the following by referring separately to the three different facilities. An exhaustive description of the performances of the various components of beam delivery systems can be found in the literature (e.g. Refs. [17,24,29,32,34,35]). However, it is worth mentioning that the treatment dose can be delivered either with passive or active systems. Passive systems are entirely based on absorbers, scattering foils and collimators, whose thickness and shape are designed to provide the desired angular and energy distribution of the beam. These devices tailor the beam to the tumour shape by widening its angular distribution, flattening its central distribution and degrading and modulating its energy in order to deliver the dose at the desired depths. Collimators and boluses are used to conform the irradiation field to the tumour volume. The energy modulation can be performed, for example, by a rotating wheel of variable thickness called a range modulator. It is impossible to reproduce the effect of such a device with a single simulation and therefore various cases related to the different thicknesses involved should be taken into account, thus increasing the global CPU time. In the present work, energy modulation was neglected, assuming that its effect on secondary neutron production is marginal, and a single thickness of the material was considered to simulate the range modulator.

On the other hand, active systems utilize deflection magnets to scan the tumour normally to the beam axis. If a synchrotron is used to accelerate protons, modulation can be performed by continuously varying the extraction energy [23]; otherwise a passive range modulator can be used to deliver the dose at different depths. In this way the tumour is subdivided into volume elements (voxels) where single spot irradiations are carried out during the treatment. Also in this case, the entire tumour scanning cannot be simulated in one step and a single depth is taken into account, assuming that the variation of the secondary neutron dose with the voxel position inside the tumour is negligible. Secondary neutron production should be lower with active systems because less material is placed in the beam path. In the simulation geometries described below, all spaces not covered by other materials were filled with air.

2.1. Centre Antoine-Lacassagne (Nice, France)

A 65 MeV proton cyclotron is installed in this facility for the treatment of eye tumours with a passive beam delivery system on a fixed horizontal beam. The proton beam extracted from the accelerator is completely defocused upstream of the kapton vacuum window (1.3 mm thick), giving rise to a Gaussian distribution. A set of collimators select the central part of Gaussian distribution in order to approximate a uniform beam. Therefore, a parallel uniform beam was considered for the simulation source. The patient is positioned on a seat supplied with a system for head immobilization.

Fig. 1 shows a schematical view of the geometry of the beam delivery system used in the simulations. Each ionization chamber was simulated with two 5-μm thick mylar foils separated by an air layer 10 mm thick. The aperture of the patient's collimator is 2 mm in radius according to the tumour diameter considered in the simulation phantom (see Section 3).

2.2. National Accelerator Centre (Faure, South Africa)

Intracranial lesions and skull base tumours are treated at the NAC proton therapy facility with a beam delivered by a 200 MeV cyclotron. Also in this case, a passive system is used and the beam is tailored using the dual-scattering foil technique [17]. As already mentioned, secondary dose measurements were performed at this facility [7], leading to the adoption of additional shields (a concrete wall and a stainless steel ring added to the second collimator). The simulation geometry considered here refers to this new configuration. A pencil beam source of 200 MeV protons was used. A schematical view of the NAC proton beam delivery system is shown in Fig. 2. The first ionization chamber was simulated with two 5-μm thick mylar foils separated by an air gap 1 mm thick. As mentioned before, the range modulator/degrader was assumed at a fixed thickness (40 mm), which was chosen according to the depth of the tumour in the simulation phantom (see Section 3). Therefore, this device behaves only as a degrader in the simulations. The two kapton windows (1 mm thick) of the structure which contains the degrader were taken into account.

The complex structure of the multiwire ionization cham-

ber (MWIC) was approximated by considering a cylinder (0.2 mm thick, radius 60 mm) filled by tungsten at a fictitious density (0.69 g/cm^3), which was obtained by multiplying the true value (19.3 g/cm^3) by the ratio of the volume of the tungsten wires to that of the chamber. This assumption can be justified by the fact that the chamber is very thin; otherwise it would strongly perturb the beam optics. The two pairs of steering magnets were approximated by a single parallelepiped (700×200 mm^2, 200 mm thick) with an aperture (300×80 mm^2) at its centre. It should be mentioned that this approximation should have a negligible effect on secondary neutron production, while the influence of the steering magnets on the beam optics was not considered.

The complex geometry of the range monitor [35] was approximated considering a 'sandwich' structure made of three brass plates (20, 37 and 21 mm thick) separated by two air gaps 3 and 9 mm thick, respectively. As mentioned above, a stainless steel ring was added to the second collimator as an additional shield [7], extending its width to 700 mm. Three cylinders with a 100 mm radius simulate the plates of the last set of ionization chambers, i.e. the central cylinder (125 μm thick) is in aluminium and the two external cylinders are considered to be in mylar (5 μm thick). The aperture of the patient's personalized collimator has a radius of 20 mm according to the tumour dimensions set in the simulation phantom (see Section 3). The isocentre is 7 m from the vacuum window.

2.3. Paul Scherrer Institute (Villigen, Switzerland)

An isocentric gantry is installed in the proton therapy room at the PSI, with an active system performing a three-dimensional conformal irradiation, delivering the beam with the discrete spot scanning technique [29,34]. The horizontal scan, in every tumour section normal to the beam axis, is carried out by one scanning magnet, while the vertical direction is taken care of by moving the patient. Depth scanning is performed using a range shifter made of several polyethylene layers that are automatically interposed along (or extracted from) the beam. A 200 MeV parallel beam of protons was used as the simulation source. The thickness of the range shifter was considered to be fixed, thus referring to the irradiation of a single tumour section at a determined depth. The variation of secondary neutron production with tumour depth was assumed to be negligible, mainly because of the low mass number of the elements constituting the patient's tissues. Only three monitors and the range shifter interact with the beam, thus contributing to secondary neutron production.

The first monitor is placed after the vacuum window and is limited by two mylar foils (19 μm thick). Between the two foils there is an ionization chamber with two mylar plates and an aluminium collector (all 25 μm thick). The air gap between the chamber elements is 5 mm thick. The second beam monitor is analogous to the first one, but the plates and the collector are separated by air layers 10 mm thick. The third monitor is a strip chamber and was simulated with two kapton and one mylar foils (25 μm thick) separated by two air gaps 20 mm thick. A 19-μm thick mylar foil is placed at the end of the strip chamber. A vacuum gap limited by two 50-μm thick mylar foils is placed downstream. The last component is the polyethylene range shifter, which is considered to be 45 mm thick according to the tumour depth of the simulation phantom.

3. Simulation phantoms

A quite detailed computational phantom was adopted for the eye treatment facility of the Centre Antoine-Lacassagne. Simplified geometries properly discretized (i.e. subdivided into cells) were considered in the other cases, as the main aim of this work is to provide an estimate of the secondary neutron and photon dose in healthy tissues during proton therapy and not to give detailed information (e.g. isodose curves) on real treatment. The phantoms are described in the following by referring separately to the different treatments taken into account.

3.1. Eye treatment – CAL

The computational phantom accounts for the organs that should be mostly exposed to secondaries. Therefore, the treated and non-treated eyes, the optical nerve sites, the skull and the brain were taken into account. The eye and skull dimensions were taken from Refs. [20,22]. The distance between the phantom eyes, the position and volume of the optic nerve site and other dimensions were obtained from a detailed analysis of CT images of the archive of the Istituto Europeo di Oncologia (European Institute of Oncology, Milano, Italy). The brain and skull bone compositions were taken from Ref. [22], while the eyes were simulated with water. Soft tissue [22] was considered to fill the optic nerve site.

The eye radius is 12 mm. A spherical cell (radius 2.5 mm), simulating the tumour, was placed at the centre of the irradiated eye. The skull and the brain cells were limited by ellipsoids, whose dimensions were taken from Ref. [20]. The major and minor axes, corresponding to the average maximum dimensions of the skull of a European male, were 185 and 144 mm, respectively. The skull bone was considered to be 5 mm thick from the analysis of the CT images mentioned above. The brain was subdivided into two symmetric parts with respect to the median sagittal plan in order to discriminate the region behind the irradiated eye.

The same geometry was considered in a further set of simulations with an Alderson phantom (type ART), which were compared with the measurements described in Section 5. The bone composition was unchanged, while that of the other cells corresponded to the Alderson muscle [21]. The

brain cell was subdivided into different zones according to the dimensions of the sections of the Alderson phantom used in the measurements.

3.2. Deep tumour treatment – NAC and PSI

In both cases, a 300-mm thick cylindrical water phantom with a 150 mm radius was used. In particular, the NAC phantom was axially subdivided into cylindrical cells 10 mm thick, which in turn were radially subdivided into concentric rings 10 mm wide. The centre of the tumour (20 mm thick, radius 20 mm) was placed at a depth of 70 mm.

The cylinder used in the PSI simulations was subdivided into various disks 10 mm thick. The tumour cell was simulated with a 30-mm thick cylinder with a radius of 30 mm, whose centre was placed at a depth of 210 mm inside the phantom. The tumour radius was 10 mm larger than that of the source parallel beam and included the lateral penumbra. It should be noted that this is different from a therapeutic situation where the target region is smaller than the irradiation beam section. The tumour cell was set in order to discriminate the proton contribution from that of the secondary neutrons.

4. Simulation results

Every result of the FLUKA simulations discussed below and listed in Table 1, 2, 3 and 4 was calculated as the mean value of the outcomes of five independent runs, each one starting with a different random seed. The uncertainties (1σ) are only statistical and were estimated from the related sample variances of the mean values. The results of the simulations are discussed below, referring separately to the considered beam delivery system configurations.

4.1. CAL

As mentioned in Section 2, the thickness of the range modulator (16 mm) and the collimator aperture (radius 2 mm) were fixed to fit the tumour depth and radius. The first set of simulations was performed to check these constraints. The 85% of the proton current density (protons per cm^2) downstream from the patient's collimator was within 2 mm from the beam axis, while the remainder was included within 3 mm. Fig. 3 shows the simulated depth dose distribution compared with that measured at the CAL with the same range shifter and collimator dimensions. It should be noted that the Bragg peak maximum was at 12 mm, corresponding to the centre of the simulated phantom eye.

The resulting values of the physical dose absorbed in the different regions of the simulation phantom normalized per therapy Gy are listed in Table 1. In particular, the total dose (protons, neutrons and photons) and that deposited by secondary photons are given separately. It should be noted that the dose absorbed in the tumour and in the irradiated eye are mainly due to the proton beam. As the beam is completely stopped in the tumour, only secondaries deliver a dose to the remaining regions. The maximum value was found in the optic nerve site behind the irradiated eye (1.1×10^{-4} Gy per therapy Gy). Further simulations were performed to estimate the energy distribution of the neutron fluence in different regions inside the phantom. The resulting spectra are characterized by almost the same behaviour below about 15 MeV. Higher energy components were observed in the treated eye and in its optic nerve site and were not scored in the related non-treated zones. A small contribution of neutrons above 15 MeV was also detected in the brain. These components, due to neutrons produced in the beam delivery system and in the treated eye, were scored with higher efficiency in this zone because of its larger dimensions. The energy distribution in the brain was found to be softer than in the eyes and in the optic nerve sites because of neutron slowing-down (scattering). It is likely that a larger discretization of the brain should have emphasized some differences in the sections close to the irradiated eye. It should be pointed out that the results refer to 1.5×10^7 particle histories (about 1 week of CPU with an ALPHA Digital™

Table 1
Dose (Gy per therapy Gy) in the simulation phantom for the eye treatment facility at the Centre Antoine-Lacassagne (Nice, France)

Region	Total dose (Gy per therapy Gy)	Relative uncertainty	Photon dose (Gy per therapy Gy)	Relative uncertainty
Tumour	1[a]	5.4×10^{-3}	–	–
Irradiated eye (tumour excluded)	2.200×10^{-2}[a]	8.4×10^{-3}	1.173×10^{-6}	2.2×10^{-1}
Non-irradiated eye	3.969×10^{-6}[b]	3.4×10^{-1}	1.554×10^{-6}	1.8×10^{-1}
Brain (behind the irradiated eye)	1.919×10^{-6}[b]	6.5×10^{-2}	5.038×10^{-7}	7.0×10^{-2}
Brain (behind the non-irradiated eye)	2.130×10^{-6}[b]	8.7×10^{-2}	5.864×10^{-7}	3.8×10^{-1}
Skull	4.577×10^{-6}[b]	8.9×10^{-2}	8.108×10^{-7}	1.1×10^{-2}
Site of the optic nerve below the irradiated eye	1.131×10^{-4}[b]	2.4×10^{-1}	7.631×10^{-7}	3.1×10^{-1}
Site of the optic nerve below the non-irradiated eye	3.819×10^{-6}[b]	3.3×10^{-1}	8.943×10^{-7}	2.7×10^{-1}

[a]Protons, neutrons and photons.
[b]Neutrons and photons.

Table 2

Total dose per therapy Gy (in a cylindrical tumour with a radius of 2 cm and a height of 2 cm) in the simulation phantom for the proton therapy facility at the National Accelerator Centre (Faure, South Africa)

	Dose due to protons, neutrons and photons						Dose due to neutrons and photons							
R (cm)	0–1		1–2		2–3		3–4		4–5		5–10		10–15	
Z (cm)	Dose (Gy)	Relative uncertainty	Dose (Gy)	Relative uncertainty	Dose (Gy)	Relative uncertainty	Dose (Gy)	Relative uncertainty	Dose (Gy)	Relative uncertainty	Dose (Gy)	Relative uncertainty	Dose (Gy)	Relative uncertainty
0–1	5.47×10^{-1}	2.88×10^{-2}	4.91×10^{-1}	1.18×10^{-2}	9.47×10^{-2}	3.63×10^{-2}	5.87×10^{-3}	1.00×10^{-1}	3.39×10^{-3}	1.59×10^{-1}				
1–2	5.57×10^{-1}	4.04×10^{-2}	5.05×10^{-1}	1.89×10^{-2}	1.04×10^{-1}	3.60×10^{-2}	5.36×10^{-3}	1.07×10^{-1}	2.45×10^{-3}	1.23×10^{-1}	9.50×10^{-4}	1.31x10^{-1}	1.46×10^{-4}	1.72×10^{-1}
2–3	6.06×10^{-1}	3.72×10^{-2}	5.44×10^{-1}	2.16×10^{-2}	1.11×10^{-1}	2.91×10^{-2}	6.17×10^{-3}	1.14×10^{-1}	2.50×10^{-3}	1.99×10^{-1}				
3–4	6.31×10^{-1}	4.29×10^{-2}	5.48×10^{-1}	2.07×10^{-2}	1.99×10^{-1}	2.67×10^{-2}	6.17×10^{-3}	1.07×10^{-1}	2.28×10^{-3}	3.72×10^{-1}				
4–5	7.06×10^{-1}	3.62×10^{-2}	6.03×10^{-1}	1.27×10^{-2}	1.38×10^{-1}	2.40×10^{-2}	6.76×10^{-3}	9.80×10^{-2}	1.90×10^{-3}	2.02×10^{-1}	3.83×10^{-4}	1.96x10^{-1}	9.47×10^{-5}	1.01×10^{-1}
5–6	8.12×10^{-1}	2.46×10^{-2}	6.75×10^{-1}	2.23×10^{-2}	1.57×10^{-1}	1.75×10^{-2}	8.39×10^{-3}	1.30×10^{-2}	1.85×10^{-3}	2.95×10^{-1}				
6–7					1.91×10^{-1}	2.04×10^{-2}	1.15×10^{-2}	9.58×10^{-2}	2.41×10^{-3}	1.47×10^{-1}				
7–8		Tumour	1 Gy		2.91×10^{-1}	4.74×10^{-3}	1.26×10^{-2}	1.33×10^{-1}	1.18×10^{-3}	7.46×10^{-2}	1.84×10^{-4}	2.38x10^{-1}	7.09×10^{-5}	1.26×10^{-1}
8–9	6.37×10^{-1}	2.25×10^{-2}	5.45×10^{-1}	1.48×10^{-2}	1.31×10^{-1}	1.19×10^{-2}	3.02×10^{-3}	2.43×10^{-1}	–	–				
9–30					$< 3.0 \times 10^{-4}$							$< 8.0 \times 10^{-5}$		

R is the radial distance from the beam axis and Z is the depth from the phantom surface (see text).

Table 3

Calculated (this work) and experimental [7] dose due to secondaries for the NAC facility (see text)

Measured (on-axis) [7]		Calculated (2–3 cm off-axis) (this work)	
Depth (cm)	Secondary dose (Gy per therapy Gy)	Depth (cm)	Secondary dose (Gy per therapy Gy)
0	1.68×10^{-2}	0–1	$(1.84 \pm 1.45) \times 10^{-2}$
0.4	2.07×10^{-2}		
0.5	2.22×10^{-2}		
1.0	2.15×10^{-2}		
1.5	2.09×10^{-2}	1–2	$(1.78 \pm 1.61) \times 10^{-2}$
2.0	1.99×10^{-2}		
5.0	1.73×10^{-2}	4–5	$(2.66 \pm 1.33) \times 10^{-2}$

workstation). A more detailed spatial discretization would have led to an unacceptably long computing time in order to achieve satisfactory statistics. Moreover, due to the geometry of the problem, the use of variance reduction techniques would have been quite critical and the risk of introducing biases would have been difficult to estimate.

The influence of the beam delivery system on the absorbed dose was investigated in another set of simulations, in which all the beam line components were neglected. The energy (36 MeV) adopted for the source proton beam corresponds to that immediately downstream from the patient collimator (calculated in the simulation with the complete beam delivery system), thus guaranteeing that the Bragg peak lays within the tumour. The dose absorbed in the different regions of the phantom (excluding the tumour) in the configuration without the beam delivery system was lower than 1% of the values listed in Table 1, thus emphasizing that the secondaries produced in the irradiated eye give a negligible contribution to the total value.

Further simulations with the same configuration of the beam delivery system and phantom geometry were performed with the LCS code [30] for comparison. The nuclear models used in this code in the energy region of interest of the present work do not differ substantially from those utilized in FLUKA. As far as neutron transport below 20 MeV is concerned, LCS links to HMCNP (a modified version of MCNP [8]) with a large set of cross-sections available (in the present work, continuous energy cross-sections were used), while FLUKA makes use of a discrete energy cross-section file with 72 groups. The total (neutrons +

Table 4

Total and secondary uncharged particle dose per therapy Gy (in a cylindrical tumour with a radius of 3 cm and a height of 3 cm) in the simulation phantom for the proton therapy facility at the Paul Scherrer Institute (Villigen, Switzerland)

Depth (cm)	Total dose ($\times 10^2$) (Gy per therapy Gy)	Relative uncertainty	Secondary uncharged particle dose ($\times 10^2$) (Gy per therapy Gy)	Relative uncertainty
0–1	38.68	2.40×10^{-4}	0.15	1.317×10^{-1}
1–2	40.04	3.31×10^{-4}	0.18	2.124×10^{-1}
2–3	41.12	1.62×10^{-4}	0.15	3.209×10^{-1}
3–4	42.12	1.86×10^{-4}	0.14	2.505×10^{-1}
4–5	43.07	2.67×10^{-4}	0.23	2.028×10^{-1}
5–6	44.00	2.32×10^{-4}	0.25	1.237×10^{-1}
6–7	44.97	1.54×10^{-4}	0.28	7.38×10^{-2}
7–8	45.96	1.91×10^{-4}	0.33	1.281×10^{-1}
8–9	47.01	7.81×10^{-5}	0.36	1.435×10^{-1}
9–10	48.16	1.56×10^{-4}	0.38	1.198×10^{-1}
10–11	49.39	2.18×10^{-4}	0.39	1.498×10^{-1}
11–12	50.80	1.35×10^{-4}	0.48	6.71×10^{-2}
12–13	52.38	1.17×10^{-4}	0.46	9.60×10^{-2}
13–14	54.23	1.43×10^{-4}	0.50	6.93×10^{-2}
14–15	56.39	1.04×10^{-4}	0.41	8.31×10^{-2}
15–16	59.04	1.51×10^{-4}	0.48	1.37×10^{-1}
16–17	62.46	1.05×10^{-4}	0.47	2.51×10^{-2}
17–18	67.07	1.94×10^{-4}	0.39	8.71×10^{-2}
18–19	73.43	1.56×10^{-4}	0.36	1.307×10^{-1}
19–22	100	1.14×10^{-4}	0.33	1.5×10^{-1}
22–23	0.34	4.54×10^{-3}	0.34	4.54×10^{-3}
23–24	0.31	8.89×10^{-3}	0.31	8.89×10^{-3}
24–25	0.29	1.06×10^{-2}	0.29	1.06×10^{-2}
25–26	0.27	6.92×10^{-3}	0.27	6.92×10^{-3}
26–27	0.25	3.61×10^{-3}	0.25	3.61×10^{-3}
27–28	0.23	9.63×10^{-3}	0.23	9.63×10^{-3}
28–29	0.22	5.02×10^{-3}	0.22	5.02×10^{-3}
29–30	0.20	9.49×10^{-3}	0.20	9.49×10^{-3}

photons) dose absorbed in the part of the brain behind the non-irradiated and the irradiated eye was $(1.94 \pm 0.14) \times 10^{-6}$ Gy per therapy Gy (FLUKA $(2.13 \pm 0.18) \times 10^{-6}$ Gy per therapy Gy) and $(1.39 \pm 0.14) \times 10^{-6}$ Gy per therapy Gy (FLUKA $(1.92 \pm 0.12) \times 10^{-6}$ Gy per therapy Gy), respectively. In the LCS calculations, the neutron component was only scored below 20 MeV. The agreement with the FLUKA results is satisfactory for the part of the brain behind the non-treated eye, while for the treated eye, the difference may be explained by the contribution of neutrons above 20 MeV.

Finally, a set of simulations was performed to investigate

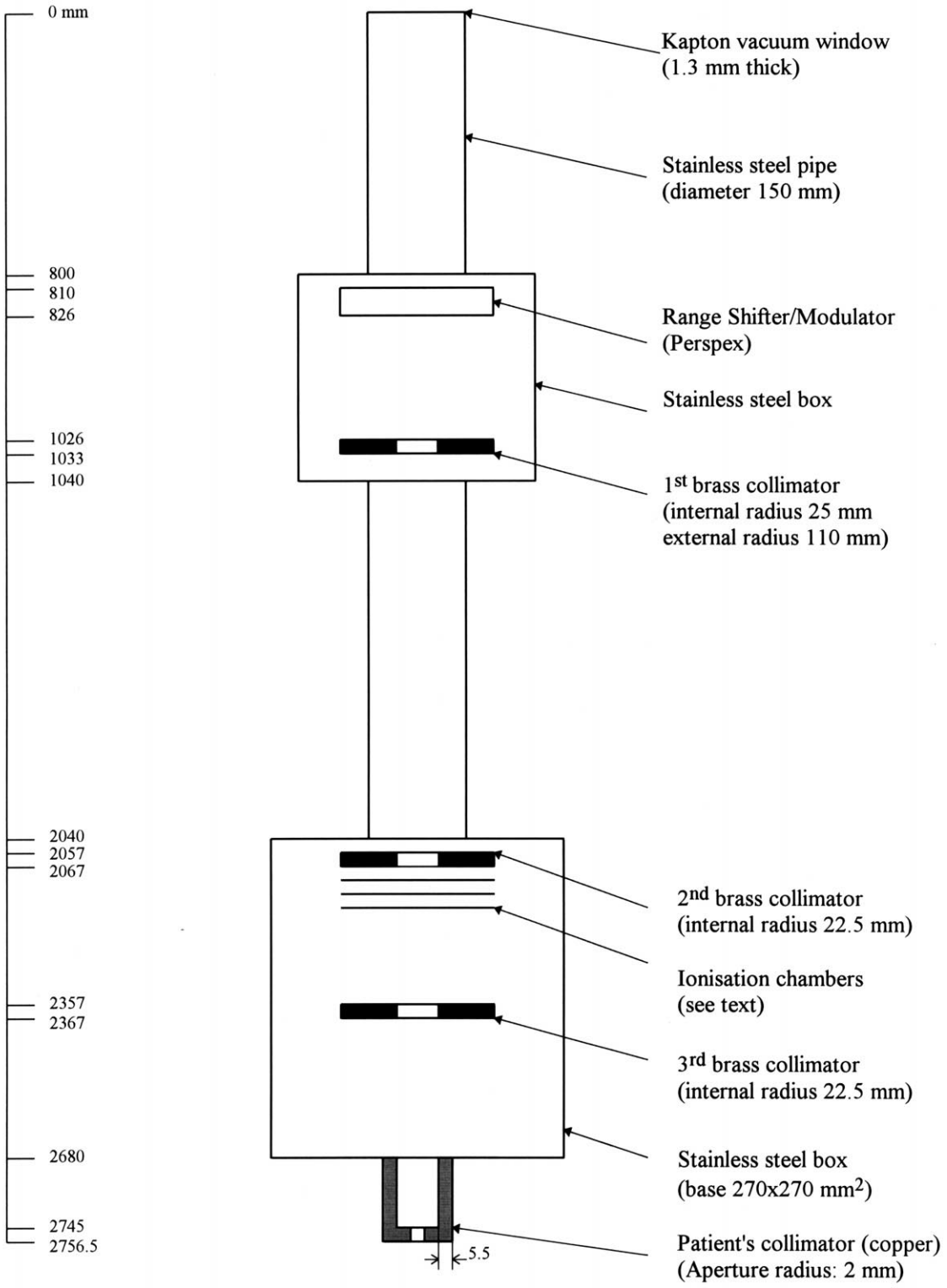

Fig. 1. Schematical view of the simulation geometry of the beam delivery system at the CAL (not to scale). Dimensions are in mm.

the influence of the various components of the beam delivery system on secondary neutron production. The neutron current (i.e. the number of particles crossing a surface) was scored on a fictitious sphere with a radius of 14 m containing the whole beam delivery system. Starting from the vacuum window, each component was added downstream in a series of separate simulations. The energy distribution of the produced neutrons is shown in Fig. 4. The component below 10 keV was neglected in curve (a) because it represents a very low contribution and the related statistics were poor. It should be noted that the first collimator (curve (c), Fig. 4) slightly increases the neutron component between 100 keV

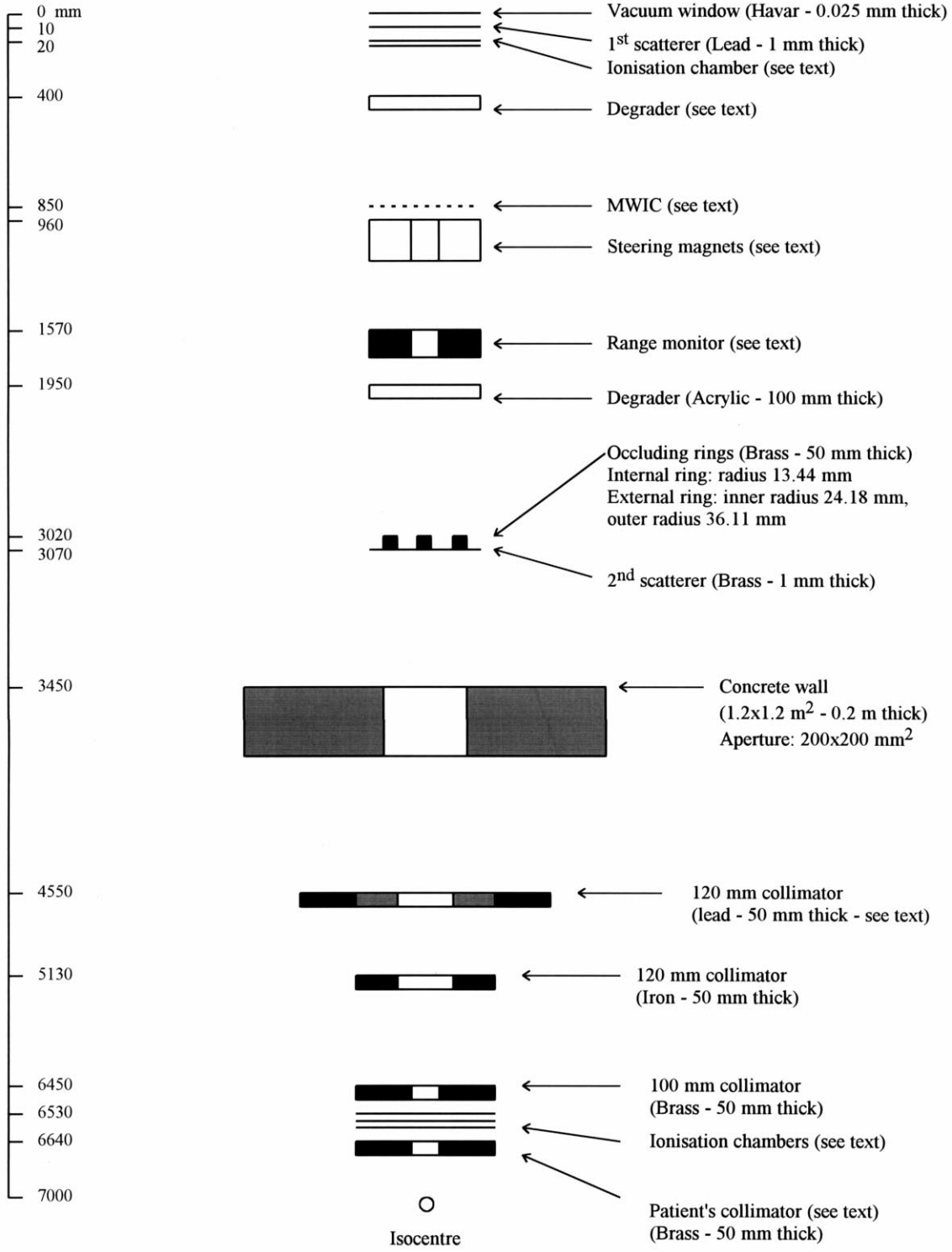

Fig. 2. Schematical view of the simulation geometry of the beam delivery system at the NAC (not to scale). Dimensions are in mm.

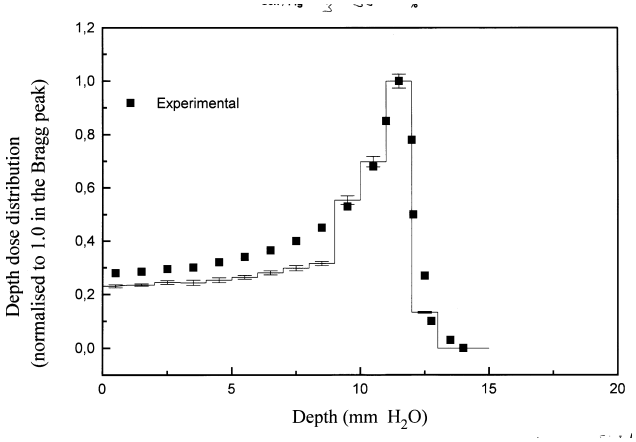

Fig. 3. Calculated and measured depth dose distributions of protons in the configuration adopted for the eye treatment system at the CAL.

and 5 MeV. This component is further increased when the pair of collimators in the second stainless steel box are added (curve (d), Fig. 4). As expected, no differences are observed when the ionization chambers are considered (curve (e), Fig. 4). The patient's collimator gives a further low contribution to the energy interval (100 keV–5 MeV) (curve (f), Fig. 4). As was expected, the components made of heavier materials and/or with large thickness are mainly responsible for secondary neutron production.

The simulations referring to the Alderson phantom used in the measurements are described in Section 5.

4.2. NAC

Also in this case, the first set of simulations was performed to check the position of the Bragg peak with respect to the tumour volume together with the lateral distribution of the proton beam before it impinges on the phantom. In particular, a flat lateral distribution was observed within the aperture of the patient's collimator, thus confirming that the effect of the dual foil scattering system was simulated correctly and that the approximations in the structure of some components of the beam delivery system (Section 2) have a small effect on the beam shaping.

The total dose values per therapy Gy are listed in Table 2. It should be pointed out that the dose up to a depth of about 10 cm and up to a radius of about 4 cm is mainly due to primary protons. In particular, the lateral penumbra is included in the region between 2 and 4 cm, but its extension

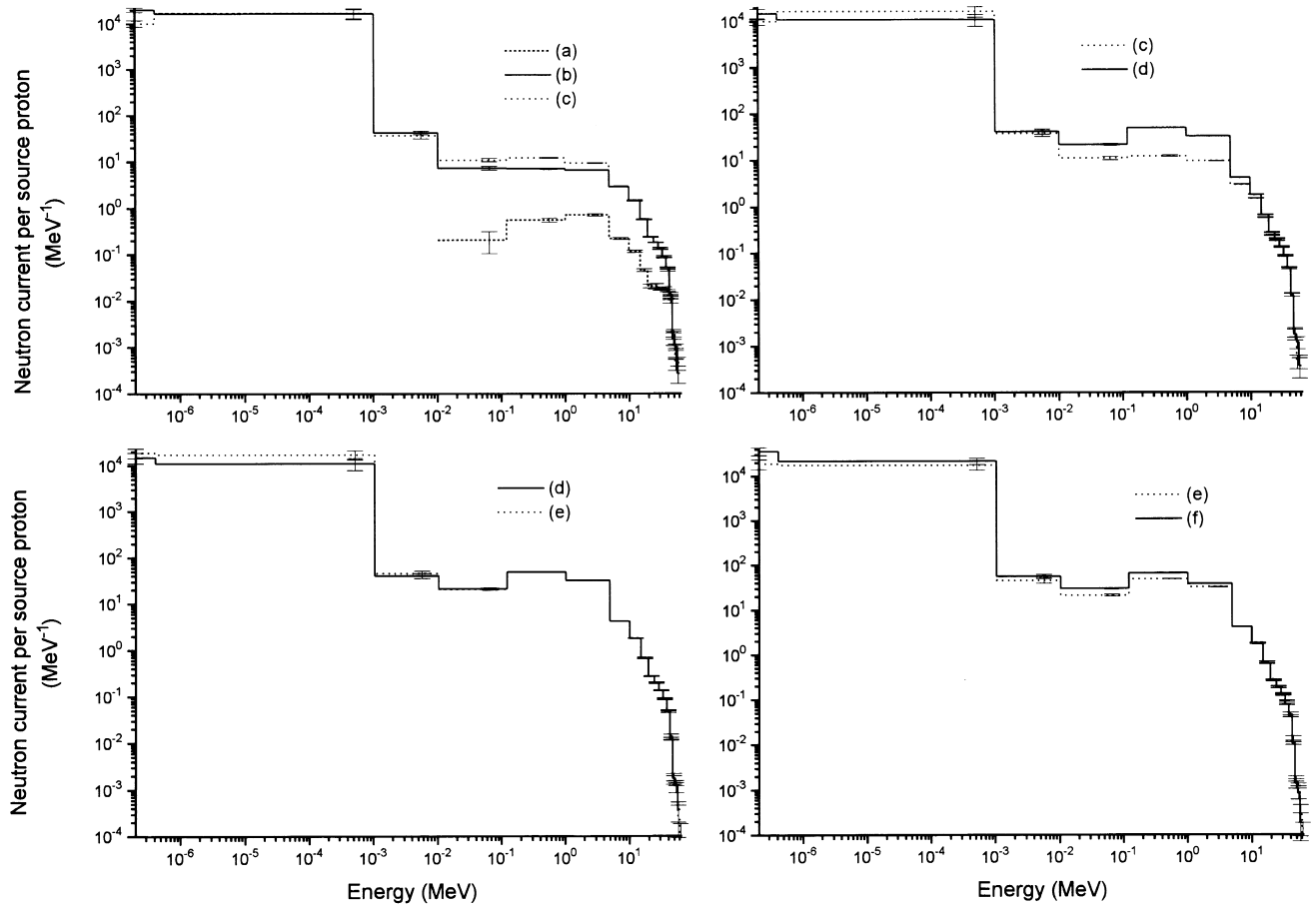

Fig. 4. Energy distributions of secondary neutrons produced in the various structural components of the nozzle at the CAL. (a) Vacuum window; (b) = (a) + range shifter; (c) = (b) + first collimator; (d) = (c) + two collimators; (e) = (d) + ionization chambers; (f) = (e) + patient's personalized collimator.

Table 5
Calculated and measured neutron fluence rates inside the Alderson phantom head irradiated at the CAL[a]

Alderson phantom section	Energy	Calculated fluence rate (cm^{-2}/s)	Fluence rate (cm^{-2}/s)	Absolute counting uncertainty	Absolute normalization uncertainty
0–1[b]	<0.4 eV	$(9.18 \pm 1.82) \times 10^3$	8.26×10^3	1.89×10^2	6.21×10^2
0–1[b]	0.4 eV–10 keV	$(3.92 \pm 0.31) \times 10^3$	3.15×10^3	1.68×10^2	2.36×10^2
0–1[c]	<0.4 eV	$(9.61 \pm 0.91) \times 10^3$	8.23×10^3	1.89×10^2	6.25×10^2
0–1[c]	0.4 eV–10 keV	$(6.48 \pm 0.34) \times 10^3$	3.66×10^3	2.34×10^2	2.81×10^2
1–2[b]	<0.4 eV	$(1.280 \pm 0.19) \times 10^4$	1.092×10^4	2.16×10^2	7.16×10^2
1–2[b]	0.4 eV–10 keV	$(5.51 \pm 0.26) \times 10^3$	3.10×10^3	1.92×10^2	2.27×10^2
1–2[c]	<0.4 eV	$(1.65 \pm 0.13) \times 10^4$	9.60×10^3	2.24×10^2	8.21×10^2
1–2[c]	0.4 eV–10 keV	$(6.76 \pm 0.26) \times 10^3$	2.39×10^3	1.89×10^2	2.15×10^2
2–3[b]	<0.4 eV	$(1.300 \pm 0.103) \times 10^4$	1.160×10^4	2.25×10^2	8.28×10^2
2–3[b]	0.4 eV–10 keV	$(5.16 \pm 0.28) \times 10^3$	3.17×10^3	2.15×10^2	2.93×10^2
2–3[c]	<0.4 eV	$(1.620 \pm 0.034) \times 10^4$	1.331×10^4	2.44×10^2	8.85×10^2
2–3[c]	0.4 eV–10 keV	$(5.90 \pm 0.31) \times 10^3$	2.36×10^3	2.06×10^2	1.84×10^2
3–4[b]	<0.4 eV	$(9.12 \pm 1.11) \times 10^3$	9.86×10^3	2.07×10^2	6.86×10^2
3–4[b]	0.4 eV–10 keV	$(5.41 \pm 0.27) \times 10^3$	2.60×10^3	2.15×10^2	8.29×10^2
3–4[c]	<0.4 eV	$(1.514 \pm 0.233) \times 10^4$	8.53×10^3	1.90×10^2	6.79×10^2
3–4[c]	0.4 eV–10 keV	$(5.97 \pm 0.36) \times 10^3$	4.98×10^3	2.59×10^2	4.05×10^2

[a]The measurement positions were between two contiguous sections of the head of the Alderson phantom. Section 0 is at the top of the skull and each section is 2.5 cm thick.
[b]Regions behind the non-irradiated eye.
[c]Regions behind the irradiated eye.

cannot be estimated with precision because of the spatial discretization of the phantom. Outside this region, where neutrons are slowed down and the contribution of protons tends to zero, the dose is within 10^{-3}–10^{-5} Gy per therapy Gy. It should be emphasized that the uncertainty of the calculated dose in the interval of 9–30 cm (depth) and within 5 cm (radius) is large and therefore this value has to be considered as merely indicative. More accurate results would have required the use of variance reduction techniques, with the risk of introducing biases which would have been difficult to estimate.

A second simulation was performed by switching off neutron and photon production in order to estimate the contribution of the secondaries by subtraction. Results of secondary neutron measurements with a tissue equivalent proportional counter (TEPC) in a solid nylon phantom are given in Ref. [7]. In that work, the patient's collimator aperture was blocked with a brass plug to completely stop the proton beam and measure only the neutron component. The difference between the total dose and the proton dose estimated at various depths of the simulation phantom and within 2 and 3 cm off-axis are listed in Table 3 together with the experimental data of Ref. [7]. The radial interval of 2–3 cm was chosen for the simulation because it is shadowed by the patient's collimator and it can be compared with the experimental situation with the beam aperture blocked. The difference between the two situations is given by the additional contribution to neutron production of the central part of the blocked collimator. As the most energetic neutrons produced in the collimator are forward directed, the dose absorbed in the phantom in the central part of the collimator should be comparable to that absorbed 2–3 cm off-axis. The simulation data listed in Table 3 are normalized to the beam intensity of 15 nA at the beam line entrance, corresponding to a dose rate of 3 Gy min^{-1} specified at the entrance plateau of the unmodulated beam at a depth of 5 cm in water [7]. This normalization was adopted to match the results of Ref. [7] and is different from that used in Table 2, where the dose scored in a cylindrical tumour (radius 2 cm, thickness 2 cm) was taken into account. It should be noted that the uncertainties of the simulation results listed in Table 3 are quite large because they refer to differences between close values (the proton dose is about 100 larger than the neutron dose), characterized by errors lower than 2%.

The doses calculated in the regions behind the patient's collimator (2–3 cm off-axis) are of the same order of magnitude (10^{-2} Gy per therapy Gy) of those measured in Ref. [7], referring to the configuration without additional shielding. By contrast, the simulated results in the regions above 3 cm off-axis are substantially lower (up to a factor 10^2) than those measured at the NAC (of the order of 10^{-2} Gy per therapy Gy, Table 2 of Ref. [7]) from 15 to 120 cm off-axis. This difference should be explained by the effect of the additional shields recently added at the NAC that, as mentioned above, were taken into account in the simulations of the present work. In the regions close to the beam axis, the secondary uncharged particle dose is mainly ruled by neutrons produced in the patient's collimator.

4.3. PSI

The total dose absorbed in the various regions of the phantom, normalized to 1 therapy Gy, are listed in Table 4. Also in this case, an additional simulation was performed by switching off neutron and photon production in order to

separate the contribution of secondary neutrons and photons. The differences between the results of the simulations are listed in Table 4. It should be noted that the uncertainties are lower than those related to the NAC because the PSI simulation geometry was less complex and almost all the source particles interacted with the phantom.

The secondary dose is in the range $(1–5) \times 10^{-3}$ Gy per therapy Gy, which is one order of magnitude lower than that estimated downstream from the NAC patient's collimator, thus confirming the lower neutron production in active beam delivery systems. The secondary photon dose was estimated to be about one tenth of the total (neutrons + photons) value. It should be noted that the secondary dose is characterized by a build-up effect showing a maximum value at a depth of about 17 cm. This behaviour is also reported in Ref. [7], although the maximum value was measured at 5 mm. It should be emphasized that these configurations cannot be compared because the PSI active system is only slightly influenced by its components (beam monitors) and the secondary neutrons are mainly produced inside the phantom, while in the case of the NAC passive beam delivery system, the secondary dose is likely to be dominated by neutrons generated in the last collimator. The build-up peak characterizing the absorption of the neutron dose corresponds to the point where the particle equilibrium of the recoil protons is achieved [7].

5. Experimental

The neutron fluence rate inside an Alderson phantom was measured at the eye treatment facility of the Centre Antoine-Lacassagne (Nice). In particular, the eye of the phantom was centred on the beam axis and a 16.5-mm thick perspex absorber was placed in the beam delivery system in order to position the Bragg peak at a depth of 12 mm according to the simulation geometry (Section 3). Fig. 3 shows the dose depth distribution measured at the CAL in the experimental configuration. An unmodulated beam was used and the radius of the aperture of the patient's personalized collimator was 2.5 mm. A set of simulations was performed with FLUKA by further subdividing the phantom brain cells according to the dimensions of the Alderson sections. All materials (skull bone excluded) were substituted with the Alderson muscle [21]. The measurement positions were between two contiguous sections of the head of the Alderson phantom. In particular, section n. 0 is at the top of the skull and each section is 2.5 cm thick. The walls of the treatment room were considered in this set of simulations in which the thermal and epithermal fluences were scored in each section of the phantom.

The thermal and epithermal (0.4 eV–10 keV) fluence rates in various positions inside the Alderson phantom head were measured with bare and cadmium-covered indium foils. The activity of the irradiated foils was measured with a 2×2" NaI(Tl) scintillator. A BF_3 proportional counter was placed at a fixed position to control the reproducibility of the irradiation conditions. Six indium foils were symmetrically placed in each phantom section with respect to the median sagittal plane. In this way, two pairs of three foils were behind the irradiated and non-irradiated eye. The results of the simulations and of the measurements (together with the related 1σ counting and normalization uncertainties) are listed in Table 5. As the simulations referred to the fluence averaged in each half of the phantom section, the experimental results in Table 5 are averaged over the fluences obtained from each set of three foils.

The normalization uncertainties were estimated by assuming a uniform probability for every source of bias [10] and their joint probability distribution was assessed with the Monte Carlo method (sampling random numbers in the interval within each bias is limited) following the procedure described in Ref. [3]. This method was adopted as the number of measured positions and the long irradiation times (about 1 h for each Alderson phantom section) did not permit repeated measurements. The normalization uncertainty sources considered were as follows: (i) NaI scintillator peak efficiency, which was estimated with MCNP simulations. The random number interval is limited by the value calculated with the indium foil strictly contiguous to the aluminium cover of the scintillator and by that with the foil at a distance of 1 mm; (ii) thermal flux depression factor, which was estimated with Monte Carlo simulations. The random number interval is limited by the values estimated for the thinner and the thicker foils used in the measurements; (iii) epithermal flux depression factor, which was estimated with Monte Carlo simulations performed with both the MCNP and FLUKA codes. In particular, as only neutron dosimetry cross-sections were available for indium in the adopted MCNP libraries, the infinitely thin target reaction rate was calculated with MCNP in the Alderson phantom (using the energy distribution of curve (f) in Fig. 4 as the neutron source) and those related to the thicker and the thinner targets used in the measurements were estimated with FLUKA; (iv) foil weight, an uncertainty of 1 LSB (least significative bit) was given, as a digital scale was used; (v)

$$\sigma_{\text{eff}} = \int_{0.4\text{ eV}}^{10\text{ keV}} \sigma(E)\Phi(E)\mathrm{d}E \Big/ \int_{0.4\text{ eV}}^{10\text{ keV}} \Phi(E)\mathrm{d}E$$

where $\sigma(E)$ is the indium absorption cross-section and $\Phi(E)$ is the neutron fluence inside the phantom. This effective cross-section was estimated with MCNP simulations as the ratio of the infinitely thin target reaction rate to the fluence rate in the Alderson phantom between 0.4 eV and 10 keV; (vi) cadmium correction factor F_{Cd}, which was estimated from Ref. [31]. The random number interval is limited by the values estimated for the thinner and thicker foils used in the measurements; (vii) a further uncertainty of 5% was conservatively assigned to the recorded counts

to account for other sources of bias (such as foil positioning, irradiation and waiting time) which, even when affected by low individual uncertainties, can jointly influence the result.

Further measurements were performed with a collimator with a radius of 5 mm, but no significant difference was observed in the resulting fluence rates.

6. Discussion and conclusions

The dose due to the secondaries was estimated for proton treatments of the eye and of deep-seated tumours. Generally, its contribution is lower in the healthy tissues not interested by the beam and/or distant from the target volume. The dose due to secondary uncharged particles depends on the materials and the geometry of the components of the beam delivery system, but it is also related to the energy of the primary proton beam, as it was found to be larger for the scanned proton beam (PSI) used for treating deep-seated tumours than for the passive beam delivery system related to the eye treatment (CAL). It should be pointed out that the present work refers only to the physical dose and does not take into account the RBEs.

If a treatment dose of 60 Gy was considered for the eye tumours, the maximum contribution (6.8 mGy) of the secondaries was found in the optic nerve site behind the irradiated eye, while about 0.12 mGy was absorbed in the brain. In the case of deep tumour treatments with a passive beam delivery system, the contribution of the secondaries was estimated to be of the order of 1 Gy (for a treatment dose of 60 Gy) in the regions immediately downstream from the patient's personalized collimator and in the volume directly irradiated by the proton beam and its penumbra. The dose is due to fast neutrons (above 1 MeV) produced in the collimator and in the patient. Outside these regions, where neutrons are slowed down, the dose is about 6 mGy. In the case of deep tumour treatments by an active beam delivery system, the maximum dose in the regions irradiated by the beam and its penumbra is 0.3 Gy (for 60 therapy Gy).

The agreement of the simulated neutron fluence rate inside the head of an Alderson phantom with measurements performed at the eye treatment facility of the Centre Antoine-Lacassagne is satisfactory. As thermal and epithermal fluences were scored in the same run in which the doses in the phantom were calculated, this agreement can be considered as an indicator of the accuracy of the simulation results related to the CAL. The secondary dose calculated in the phantom regions downstream from the patient's personalized collimator for the NAC configuration were found to be consistent with the measurements of Ref. [7]. In the regions off-axis not shadowed by the patient's collimator, the secondary dose was about 100 times lower than that measured in Ref. [7], thus confirming the effect of the shield recently added at the NAC.

Acknowledgements

The authors are indebted to N. Iborra-Brassart (Centre Antoine-Lacassagne, Nice, France), E. Pedroni and S. Lin (Paul Scherrer Institute, Villigen, Switzerland) and P.J. Binns (National Accelerator Centre, Faure, South Africa) for providing essential information about the beam delivery systems of their facilities and for their helpful advice. Special thanks to N. Iborra-Brassart and to the personnel of the Centre Antoine-Lacassagne for their support and advice during the measurements at their eye treatment facility. The authors also thank the referees for their useful comments.

References

[1] Agosteo, S., Foglio Para, A., Gerardi, F., Silari, M., Torresin, A. and Tosi, G. Photoneutron dose in soft tissue phantoms irradiated by 25 MV X-rays. Phys. Med. Biol. 38: 1509–1528, 1993.
[2] Agosteo, S., Foglio Para, A., Maggioni, B., Sangiust, V., Terrani, S. and Borasi, G. Radiation transport in a radiotherapy room. Health Phys. 68: 27–34, 1995.
[3] Agosteo, S., Colautti, P., Corrado, M.G., et al. Characterisation of an accelerator-based neutron source for BNCT of explanted livers. Radiat. Prot. Dosim. 70: 559–566, 1997.
[4] Amaldi, U., Arduini, G., Badano, L., et al. A hospital-based hadrontherapy complex. In: Proceedings of the Fourth European Particle Accelerator Conference, London (UK) 27 June–1 July 1994, p. 49. World Scientific, Singapore, 1994.
[5] Amaldi, U. and Silari, M. (Editors) The TERA Project and the Centre for Oncological Hadrontherapy, 2nd edn. INFN-LNF, Frascati, Roma, 1995.
[6] Amaldi, U., Arduini, G., Badano, L., et al. The Italian project for a hadrontherapy centre. Nucl. Instrum. Methods A360: 297–301, 1995.
[7] Binns, P.J. and Hough, J.H. Secondary dose exposures during 200 MeV proton therapy. Radiat. Prot. Dosim. 70: 441–444, 1997.
[8] Briesmeister, J.F. (Editor) MCNP – A General Monte Carlo N-Particle Transport Code, Version 4A. Los Alamos National Laboratory LA-12625-M, Los Alamos, NM, 1993.
[9] Campi, D. and Silari, M. (Editors) The TERA Project and the Centre for Oncological Hadrontherapy – Updates and Revisions. INFN-LNF, Frascati, Roma, 1995.
[10] Cohen, E.R. Uncertainty and error in physical measurements. In: Proceedings of the International School of Physics 'Enrico Fermi', Course CX, p. 11. Editors: L. Crovini and T.J. Quinn. North Holland, Amsterdam, 1992.
[11] Fassò, A., Ferrari, A., Ranft, J., Sala, P.R., Stevenson, G.R. and Zazula, J.M. A comparison of FLUKA simulations with measurements of fluence and dose in calorimetric structure. Nucl. Instrum. Methods A332: 459, 1993.
[12] Fassò, A., Ferrari, A., Ranft, J., Sala, P.R., Stevenson, G.R. and Zazula, J.M. FLUKA92. In: Proceedings of the Workshop on Simulating Accelerator Radiation Environment, Santa Fe, 11–15 January 1993, p. 134. Editor: A. Palounek. Los Alamos National Laboratory LA-12835-C, Los Alamos, NM, 1994.
[13] Fassò, A., Ferrari, A., Ranft, J. and Sala, P.R. FLUKA: present status and future development. In: Proceedings of the 4th International Conference on Calorimetry in High Energy Physics, La Biodola, Italy, 21–26 September 1993, p. 493. Editors: A. Menzione and A. Scribano. World Scientific, Singapore, 1994.
[14] Fassò, A., Ferrari, A., Ranft, J. and Sala, P.R. FLUKA: performances

and applications in the intermediate energy range. In: Proceedings of the AEN/NEA Specialists' Meeting on Shielding Aspects of Accelerators, Targets and Irradiation Facilities, Arlington, Texas, 28–29 April 1994, p. 287. OECD Nuclear Energy Agency, Paris, 1995.
[15] Ferrari, A., Sala, P.R., Guaraldi, G. and Padoani, F. An improved multiple scattering model for charged particle transport. Nucl. Instrum. Methods B71: 412, 1992.
[16] Ferrari, A. and Sala, P.R. A new model for hadronic interactions at intermediate energies for the FLUKA code. In: Proceedings of the MC93 International Conference on Monte Carlo Simulation in High-Energy and Nuclear Physics, Tallahassee, 22–26 February 1993, p. 277. Editors: P. Dragovitsch, S.L. Linn and M. Burbank. World Scientific, Singapore, 1994.
[17] Grusel, E., Montelius, A., Brahme, A., Rikner, G. and Russel, K. A general solution to charged particle beam flattening using an optimized dual-scattering-foil technique, with application to proton therapy beams. Phys. Med. Biol. 39: 2201–2216, 1994.
[18] Gudowska, I. Measurement of neutron radiation around medical electron accelerators by means of ^{235}U fission chamber and indium foil activation. Radiat. Prot. Dosim. 23: 345–348, 1988.
[19] Ing, H., Nelson, W.R. and Shore, R.A. Unwanted photon and neutron radiation resulting from collimated photon beams interacting with the body of radiotherapy patients. Med. Phys. 9: 27–33, 1982.
[20] International Commission on Radiation Units and Measurements. Tissue Substitutes in Radiation Dosimetry and Measurement. ICRU Report 44. ICRU, Bethesda, MD, 1989.
[21] International Commission on Radiation Units and Measurements. Phantoms and Computational Models in Therapy, Diagnosis and Protection. ICRU Report 48. ICRU, Bethesda, MD, 1992.
[22] International Commission on Radiological Protection. Report of the Task Group on Reference Man. ICRP Publication 23. ICRP, Pergamon Press, Oxford, 1974.
[23] Kraft, G., Becher, N., Blasche, K., et al. The Darmstat program HITAG: heavy ion therapy at GSI. In: Hadrontherapy in Oncology, p. 217. Editors: U. Amaldi and B. Larsson. Excerpta Medica International Congress Series 1077. Elsevier, Amsterdam, 1994.
[24] Markovits, Ch. The OPTIS facility at PSI for the protontherapy of uveal melanomas: 9-years experience from the accelerator point of view. In: Hadrontherapy in Oncology, p. 462. Editors: U. Amaldi and B. Larsson. Excerpta Medica International Congress Series 1077. Elsevier, Amsterdam, 1994.
[25] McCall, R.C., Jenkins, T.M. and Shore, R.A. Transport of accelerator produced neutrons in a concrete room. IEEE Trans. Nucl. Sci. NS-26: 1593–1597, 1979.
[26] McGinley, P.H. Photoneutron fields in medical accelerator rooms with primary barriers constructed of concrete and metals. Health Phys. 63: 698–701, 1992.
[27] National Council on Radiation Protection and Measurements. Neutron Contamination from Medical Electron Accelerators. NCRP Report 79. NCRP, Bethesda, MD, 1979.
[28] Palta, J.R., Hogstrom, K.R. and Tannanonta, C. Neutron leakage measurements from a medical linear accelerator. Med. Phys. 11: 498–501, 1984.
[29] Pedroni, E. Beam delivery. In: Hadrontherapy in Oncology, p. 434. Editors: U. Amaldi and B. Larsson. Excerpta Medica International Congress Series 1077. Elsevier, Amsterdam, 1994.
[30] Prael, R.E. and Lichtenstein, H. User Guide to LCS: the LAHET Code System. Los Alamos National Laboratory LA-UR-89-3014, Los Alamos, NM, 1989.
[31] Price, W.J. Nuclear Radiation Detection. McGraw Hill, New York, 1964.
[32] Renner, T.R., Chu, W.T. and Ludewigt, B.A. Advantages of beam scanning and requirements of hadrontherapy facilities. In: Hadrontherapy in Oncology, p. 453. Editors: U. Amaldi and B. Larsson. Excerpta Medica International Congress Series 1077. Elsevier, Amsterdam, 1994.
[33] Sanchez, F., Madurga, G. and Arrans, R. Neutron measurements around an 18 MV linac. Radiother. Oncol. 15: 259–265, 1989.
[34] Scheib, S., Pedroni, E., Lomax, A., et al. Spot scanning with protons at PSI: experimental results and treatment planning. In: Hadrontherapy in Oncology, p. 471. Editors: U. Amaldi and B. Larsson. Excerpta Medica International Congress Series 1077. Elsevier, Amsterdam, 1994.
[35] Schreuder, A.N., Jones, D.T.L., Symons, J.E., Fulcher, T. and Kiefer, A. The NAC proton therapy beam delivery system. In: Proceedings of the 14th International Conference on Cyclotrons and their Applications, Cape Town, October 1995. World Scientific, Singapore, 1995.
[36] Sherwin, A.G., Pearson, A.J., Richards, D.J. and O'Hagan, J.B. Measurement of neutrons from high energy electron linear accelerators. Radiat. Prot. Dosim. 23: 337–340, 1988.
[37] Tosi, G., Torresin, A., Agosteo, S., et al. Neutron measurements around medical electron accelerators by active and passive detection techniques. Med. Phys. 18: 54–60, 1991.
[38] Uwamino, Y., Nakamura, T., Okubo, T. and Hara, A. Measurement and calculation of neutron leakage from a medical electron accelerator. Med. Phys. 13: 374–383, 1986.